 doi:10.20944/preprints202209.0217.v1

Article

Visualization of the Dynamic Brain Activation Pattern During a Decision Making Task

Harshit Parmar [1]* and Eric Walden [1]

[1] Texas Tech Neuroimaging Institute, Texas Tech University
* Correspondence: harshit.parmar@ttu.edu

Abstract: Decision making is a complex process involving various parts of the brain which are active during different times. It is challenging to measure externally the exact instance when any given region becomes active during the decision-making process. Here we try to extract and visualize the dynamic functional brain activation information from the observed fMRI data. We propose the use of a regularized deconvolution model to simultaneously map various activation regions within the brain and track how different activation regions changes with time. Thus, providing both spatial and temporal brain activation information. The activation information can then be further analyzed as per need and requirements. The proposed technique was validated using simulated data and then applied to a simple decision-making task for identification of various brain regions involved in different stages of decision making. The visualization aspect of the algorithm allows us to actually see the flow of activation (and deactivation) in form of a motion picture. The dynamic estimate may aid in understanding the causality of activation between various brain regions in a better way.

Keywords: decision making; dynamic activation; fMRI; visualization; deconvolution

1. Introduction

The use of functional magnetic resonance imaging (fMRI) to study the neuroscientific underpinnings of decision making has been quite popular and successful. Studies have revealed various factors that affect decision making like reward [1, 2], risk [3, 4], uncertainty [5, 6], morality [7, 8], and many others. However, these studies have relied on examining static differences in a contrast model, thereby averaging decision making across time. However, decision making is a dynamic process [9]. Unfortunately, it is challenging to design an analysis pipeline to handle continuous processes within the GLM (generalized linear model) framework.

There are numerous issues that needs to be addressed before any inference can be made from the raw fMRI time series. First, the useful blood oxygenation level dependent (BOLD) signal is only 2% - 5% the absolute intensity [10, 11]. Second, because the fMRI measures the indirect effect of neuronal activity, the neuronal signal is convolved with the hemodynamic response and is shifted in time by 4-6 seconds [12, 13]. Third, the fMRI time series is very noisy. A typical fMRI timeseries is confounded with various noise sources including physiological artifacts like cardiac and respiratory noise, motion artifact, system induced noise like gaussian and thermal noise, signal drift due to scanner instabilities and background noise [14, 15].

In traditional task fMRI data analysis, the predicted BOLD response is obtained by convolving the experiment design with the hemodynamic response function [16]. In case of decision-making studies, it is difficult to get the exact onset time of individual steps involved in the decision-making process and thus it is challenging to have an accurate experiment design that can be used to obtain a reliable predicted response. Moreover, the entire decision making is a continuous process and different parts of the brain are involved at different time instances [9, 17]. Here we propose the use of a deconvolution-based technique for estimation and visualization of the continuous dynamic brain activity

 doi:10.20944/preprints202209.0217.v1

during a simple task binary decision-making task. Instead of estimating the predicted response, the observed BOLD time series is used to obtain an estimate of the experiment paradigm for each voxel, henceforth referred as 'pseudo stimulus'. It is assumed that the pseudo-stimulus causes the observed BOLD signal changes and thus can be an accurate representation of the ongoing dynamic brain activity. The use of hemodynamic response model corrects for hemodynamic delays observed in the BOLD signal and the inference from the pseudo stimulus can be time locked to the actual experiment design. Regularization is also used to reduce the effects of noise. It is shown in the appendix section that the shape of the extracted pseudo stimulus remains close to the simulated ground truth even for low SNR observed signals.

Deconvolution models have been used for analysis of fMRI data to extract the hemodynamic response function [18, 19, 20, 21] and its variability [22]. Moreover, deconvolution models have also been used to identify underlying neural events from the observed BOLD time series [23, 24, 25]. Commonly, hemodynamic deconvolution models use lasso regularization (L1 regularization) which results in temporally sparse neuronal activity [26, 27, 28]. One of the main goals was to obtain a obtain a continuous visualization of the decision-making process while the output of L1 regularization was sparse. The decision-making task used in this study is also a block design and not event related making a continuous interpretation more useful. A variant of L1 regularization, L1 regularization of the first difference of the weight vector, was also tested (described in appendix section) and the results of that were similar to L2 regularization. Thus, L2 regularization [29] was used instead which provides a smoother (temporally) more continuous output with smaller computation time. Output of L1 regularization is also more susceptible to noise as compared to L2 regularization. Moreover, the solution to the L2 regularized cost function can be obtained using a closed form equation while the solution to L1 regularized cost function is obtained via an iterative process making L1 regularization time and resource intensive process [30]. Because of the requirements for the application and faster computation times, L2 regularization was preferred over the standard L1 regularization.

2. Materials and Methods

2.1. Algorithm

Instead of specifying a known onset time and offset time and then convolving with an HRF and estimating whether a given voxel has significant activation during the time frame, the current approach instead creates a hypothetical HRF for each time point and then tests to see which HRFs fit the data that is observed. At each time point, a question is asked, would an HRF that started here give rise to data like the data being observed? We can then find times at which an HRF in a particular voxel would have generated data like the actual data. Thus, we do not need the onset and offset time of a known stimuli. Instead, we can induce the onset and offset time of a stimuli that would give rise to the data. We call this a pseudo-stimulus.

We first explain the algorithm using a single time series and then later extended to time series of all the voxels within the brain. The entire algorithm is shown in Figure 1. The most common step in a task fMRI analysis is the generation of an estimated response time series. The estimated response is obtained by convolving the experiment design with the hemodynamic response function (HRF). In figure 1, the experiment design is shown in part (A), typical hemodynamic response is shown in part (B) and the estimated response time series is shown in black in part (E) of Figure 1. In this study, we are interested in obtaining the experiment design from the actual voxel time series. The most straight forward way of doing that is to use a deconvolution model with the observed time series and the HRF model. However, the deconvolution models are very sensitive to noise. Given the fact that the fMRI time series are very noisy, outputs of the deconvolution models are not reliable. Thus, a different approach must be used to estimate the experiment design from the observed BOLD signal.

Preprints (www.preprints.org) | NOT PEER-REVIEWED | Posted: 15 September 2022 doi:10.20944/preprints202209.0217.v1

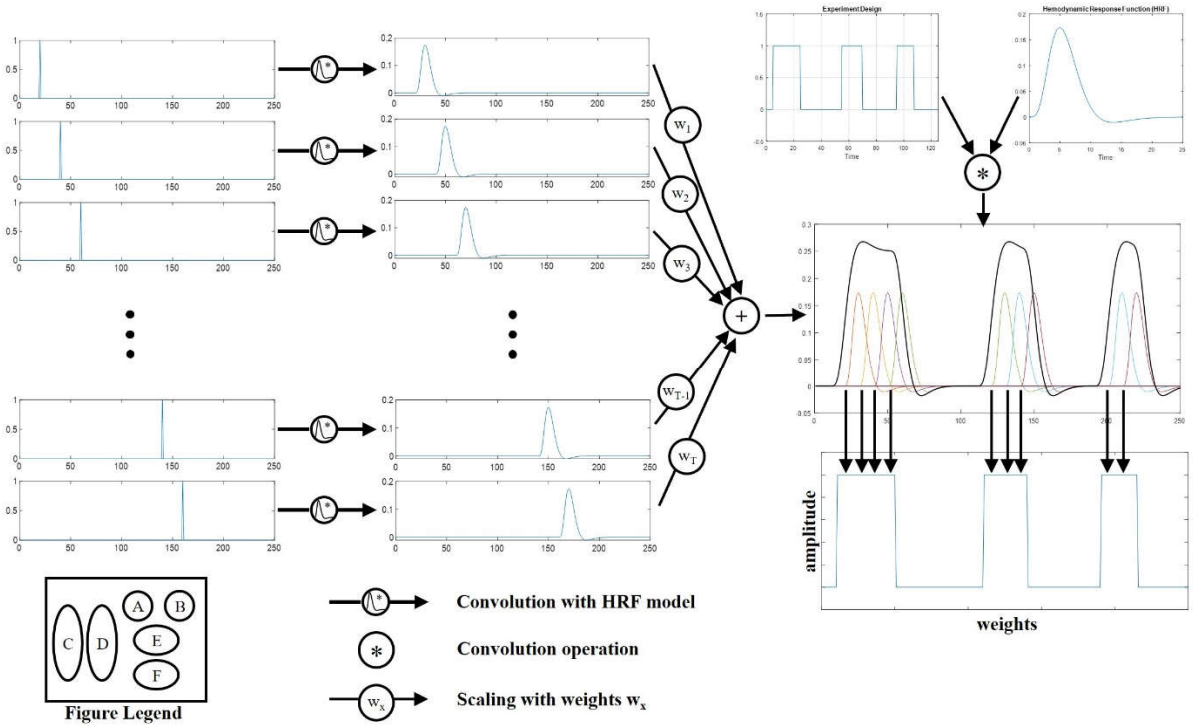

Figure 1. Summary of the algorithm for extraction of pseudo-stimulus from given time series. (A) Typical fMRI experiment design. (B) Standard double gamma hemodynamic response function (HRF). (C) Train of impulses delayed in time. The time delay between each pair of impulse is equal to 1 TR. (D) The impulse train convolved with the HRF to give time shifted hemodynamic responses. The time shifted hemodynamic responses are used as regressors in the design matrix. (E) Observed time series shown as weighted sum of time shifted hemodynamic responses. (F) Extracted pseudo-stimulus, obtained from the weights of the time shifted hemodynamic responses.

The observed signal is assumed to be a weighted sum of individual hemodynamic responses at different time instances. The colored plots in part (E) of Figure 1 shows how the predicted response can be obtained as weighted sums of hemodynamic responses at different time instances. The first step in the approach is to form the design matrix. The design matrix consists of 3 main parts. First an impulse function is generated for each TR (repetition time) (part C). This is convolved with an HRF model to form a series of hemodynamic responses that would have been generated by a pseudo-stimulus at every TR in the study (part D).

Next a set of cosine basis function which corresponds to the low frequency signal drift is added to the matrix. The number of cosine basis sets can vary depending upon the overall experiment paradigm and the total duration of fMRI acquisition. The low frequency fluctuations are generally of the order of once cycle ever 100 – 150 seconds. The smallest frequency in the cosine basis set corresponds to half cycle in entire scan duration and the remaining frequencies are integer multiples of it. The sampling frequency of the cosine basis should be set to be 1/TR Hz. Finally, the last part consists of a constant term which accounts for offset, absolute baseline intensity of the voxel. The fMRI data is pre-processed and corrected for motion and temporal signal drift. The cosine basis set and the constant terms are only to account for any residual signal bias or drift (if any) in the pre-processed data.

The linear model used for estimation of the pseudo stimulus is specified in equation 1 where Y corresponds to the observed signal, DM corresponds to the design matrix, W corresponds to the weights for the regressors (pseudo stimulus) and ε corresponds to un-modelled noise. In equation 1, DM ϵ RT x N (N = T + Nc + 1; T is the number of TR in fMRI data; Nc is the number of cosine basis sets), Y ϵ RT x Nv (Nv is the number of voxels inside the brain), and W ϵ RN x Nv. There are more features than data points, so L2 regularization also known as ridge regression [29] is used to estimate a set of weights, where the

Preprints (www.preprints.org) | NOT PEER-REVIEWED | Posted: 15 September 2022 doi:10.20944/preprints202209.0217.v1

observed activation levels are the dependent variable. The fMRI time series is noisy and with the help of L2 regularization the pseudo stimulus can be estimated with decent accuracy even at low SNR (discussed in appendix section). Equation 2 shows the optimization equation used for approximation of W where 'λ' is the regularization constant and 'I' is an identity matrix of size 'N'. Typically, for fMRI studies, different λ value is used for each voxel but here a fixed value of λ is used. A discussion about the selection of λ value and why a constant value is used for λ is discussed in the appendix section. The closed form solution for equation 2, which is used for software implementation, is shown in equation 3.

$$Y \sim DM \times W + \varepsilon$$

Equation 1

$$L(w) = \frac{1}{2N}\sum_{n=1}^{N}\left(\hat{Y}_n - Y_n\right)^2 + \frac{\lambda}{2}\sum_{n=1}^{N}\|w_n\|^2$$

Equation 2

$$\underset{W}{\operatorname{argmin}}\, L(w) \sim \left(\frac{DM^T \cdot DM}{N} + \lambda I\right)^{-1}\left(\frac{DM^T}{N} \cdot Y\right)$$

Equation 3

The size of estimated pseudo stimulus matrix W will be N x Nv, where each column corresponds to the estimated weights for a single voxel. The pseudo-stimulus for each voxel can be obtained from a subset of W including first T rows and all Nv columns. Each row in the subset of W can be converted to a 3D volume, corresponding to the size of the brain, and volumes from consecutive rows corresponds to consecutive time points (TRs). All T consecutive weight volumes can also be compiled into a single motion picture to visualize the dynamic process going on inside the brain.

2.2. Experiment Protocol

The experiment was a simple binary decision-making task where the participants had to decide whether they would download an app or not. A total of 50 different mobile applications were selected form the Google Play android app store. The apps were relatively uncommon, and a post scan survey was conducted to know how many of the apps were previously used by the participants. On average participants had used only 3 out of 50 apps, with 8 being the maximum.

Preprints (www.preprints.org) | NOT PEER-REVIEWED | Posted: 15 September 2022 doi:10.20944/preprints202209.0217.v1

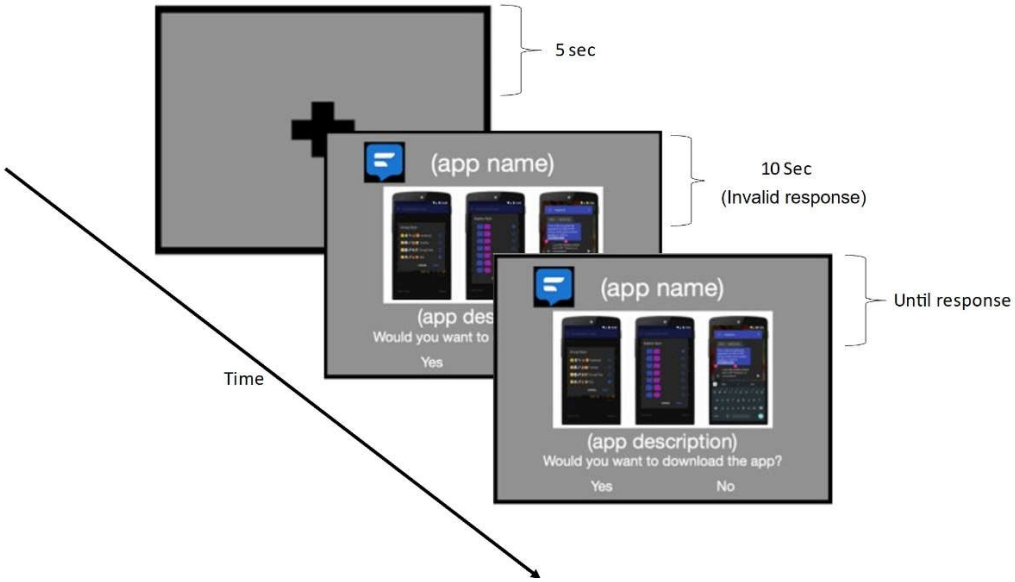

Figure 2. Representation of the experiment protocol. There is a 5 second blank screen before the beginning of the stimulus. After the stimulus starts, the response during the first 10 seconds is not considered valid. After 10 seconds, the response by the user is considered valid and it will end the stimulus bring back the blank screen before beginning the next stimulus.

When inside the scanner, anatomical images were obtained first followed by the functional scans. The task was to look at the name, logo, screenshot and a short description of the apps and decide whether to download the app or not. The responses were indicated by a button press with the right index finger for YES and right middle finger for NO. As soon as the participant presses the button, there is a blank screen with a small crosshair in the middle for 5 seconds followed by the details of the next app. The blanking period is to allow for the blood flow to return to baseline before the beginning of the next stimulus. The app order was randomized for each participant. The description of the apps was character matched so that descriptions for all the apps were between 270 to 280 characters. Also, all the descriptions were fed to a text to speech (TTS) software and the reading time of the TTS software for all the apps was between 17 and 18 seconds. Considering the 17 second time to read the text, responses were only valid 10 seconds after the beginning of the stimulus. The participants could respond before 10 seconds, but it doesn't move to the next app and those responses (trials) were not considered for analysis. Thus, a button pressed after 10 seconds initiated a change to the next app. The 10 second window allowed to discard participants and trial not performed seriously. There was no upper bound time limit, and the participants can take as long as they want to respond to a particular app. Figure 2 shows the experiment protocol for a single app.

A total of 22 undergraduate students from a large western university participated in this study. The participants received bonus course credits for their participation. There were 9 males and 12 females (one participant choose not to specify their gender) with an average age of the population being 20.86 ± 1.75 years (min = 19, max = 26). 21 out of 22 participants were right hand dominant. The participants were asked for fill out an informed consent and an MRI safety screening form prior to being in the MRI scanner. An institutional review board (IRB) approval was also obtained for the experiment. The participants were also given instructions about the task and practiced the task on a laptop outside the scanner. The practice task had the exact same user interface, but the apps used in the practice were different from the apps used in actual experiment.

The MR scans were performed on a 3T Siemens Skyra scanner. The anatomical scans were acquired using a MPRAGE pulse sequence with repetition time (TR) of 1900 milliseconds and an echo time (TE) of 2.49 milliseconds. Anatomical scans consist of 192 sagittal images (each 0.9 mm thick) with an in-plane resolution of 1mm x 1mm. The functional

Preprints (www.preprints.org) | NOT PEER-REVIEWED | Posted: 15 September 2022 doi:10.20944/preprints202209.0217.v1

scan were acquired using a multiband echoplanar imaging (MB-EPI) pulse sequence [31] with a TR of 545 milliseconds and a TE of 29 milliseconds. Each functional volume was acquired with 48 axial slices (6 slices acquired at once because of multiband) of thickness 3.3 mm and in-plane resolution of 3.25mm x 3.25mm. As the participants responded at their own pace for each stimulus, the total scan time and thus the total number of functional volumes acquired varied from 1496 (~15 mins) to 3129 (~29 mins).

2.3. fMRI Data Analysis

The preprocessing is done using SPM 12 toolbox [32] on MATLAB 2020a. The preprocessing includes

- For motion correction, rigid body affine transformation is applied to all the functional volumes to align them to the first functional volume. The rigid body transformation accounts for 6 degrees of freedom that includes 3 translation and 3 rotational motions.
- After motion correction the functional and anatomical volumes are coregistered. A 3D affine transform with 12 degrees of freedom is used to align the anatomical and mean functional volume.
- Next the images are normalized by mapping both anatomical and functional volumes onto the MNI152 brain atlas [33]. The functional volumes were mapped onto the atlas with a spatial resolution of 3mm x 3mm x 3mm while the anatomical volumes were mapped onto the atlas with spatial resolution of 1mm x 1mm x 1mm.
- Temporal signal drift was reduced and spatial smoothing was applied to all the functional volumes. Signal drift was estimated and reduced using a Principal Components Analysis based technique [34]. The spatial smoothing was performed using a 3D Gaussian kernel with a full width half maximum (FWHM) of 5 mm.
- The normalized volumes are then segmented into gray matter, white matter, cerebrospinal fluid (CSF), skull and skin. The segmented gray matter, white matter and CSF volumes are used to obtain a brain mask. Any voxels outside the brain region were discarded from further analysis to reduce the amount of data and computation time.

Before explaining each component of the estimation, we will lay out the overall process.

- Extract the pseudo stimulus for each voxel
- Normalize the response times
- Average together all of a single participants response level across all trials.
- Repeat for only the trials with a yes and only the trials with a no answer.
- Use clustering to compress the 50,000+ voxels' responses into 20 clusters.

The preprocessed data is then used to extract the pseudo-stimulus for each participant. First the entire 4D fMRI volume is converted to a 2D matrix of size T x Nv. Nv is the total number of voxels that lie within the brain region and T is total number of brain volumes in the data. Each column of this matrix corresponds to that voxel's time series. This is the matrix 'Y' as described in section 2.1. From the matrix 'Y', the weight matrix is estimated which is of size N x Nv, where N corresponds to the number of regressors in the design matrix. The first 'T' rows of the weight matrix correspond to the pseudo stimulus estimate for each of the Nv voxels. The voxel-wise pseudo-stimulus is estimated for all the participants.

The response times varied across apps and across participants thus a one-to-one comparison is not possible. All the stimuli where participants responded before 10 seconds were discarded. The average number of stimuli that were discarded per participant was 5.3 (min = 0; max = 16; median = 4). Thus, it can be assumed that all the responses were at least 10 seconds long and with 5 seconds blanking period making a total time of 15 seconds. To have uniformity in analysis, the onset of the stimulus is considered as the

Preprints (www.preprints.org) | NOT PEER-REVIEWED | Posted: 15 September 2022 doi:10.20944/preprints202209.0217.v1

reference point and 13 seconds (25 TRs, including the reference point) before and after the reference point are considered for each app. Thus, for each stimulus, a fixed length window is obtained which is centered at the onset of stimulus. This fixed window allows us to compare the response across different apps and participants. For each participant, the pseudo-stimulus in the fixed window across all the apps is averaged together to obtain a participant level response to the stimulus.

For each participant, the pseudo-stimulus is used to obtain the participant level response to the app download decision. The participant level response matrix is of size 49 x Nv (the reference point being the 25th row). Let's assume that the kth trial began at time instance tk. Corresponding to that, the time window would be [tk – (24) • TR] to [tk + (24) • TR]; for k = {1, 2, 3, …, 50}. For a given participant, all the 49 x Nv matrices (corresponding to each value of k) are averaged together to have single participant level response to the app.

The participant level response shows how the brain activity of the participant changed when responding to the app download decision. Three separate responses were obtained for each participant, one for all the apps, one for apps for which the participant decided to download (YES apps) and the last one for the apps the participant didn't decide to download (NO apps).

Finally, considering the response for each voxel as features, the voxels are clustered into 20 different groups using the k-means clustering approach. For each cluster, a representative response is obtained by grouping the voxel response for all the voxels belonging to same cluster. At the end of clustering the 49 x Nv matrix is converted to a 49 x 20 matrix with each column containing the temporal response to a single cluster.

The clustering and representative cluster response was obtained for all participants. However, the cluster assignment for k-means clustering is randomized and a correlation-based post processing step was used to match the clusters across all participants. The group level analysis was performed by combining the spatial clusters and cluster response for all participants. Useful information can be extracted from the spatial clusters and cluster-wise response.

3. Results and Discussion

The modified deconvolution algorithm was first tested on a synthetic data with single time series. Figure 3 shows the results for simulated data. Figure 3a shows the actual experiment design used to generate a synthetic time series and the estimated pseudo-stimulus. The actual experiment stimulus was convolved with the hemodynamic response function to generate the synthetic BOLD time series. Figure 3b shows the clean (black dotted) and noisy (grey) synthetic BOLD time series along with the reconstructed time series (blue) as estimated by the proposed algorithm. The noisy time series consists of thermal noise and signal drift components added to the clean signal. The estimated signal drift/baseline is also shown in figure 3b in red. From figure 3a, it can be observed that the estimated pseudo-stimulus closely follows the actual stimulus. The Pearson correlation coefficient is computed to quantify the similarity between the actual and estimated stimulus. The correlation between the actual and estimated stimulus is 0.9126. Another interesting thing to observe is that the short duration stimuli are estimated with a relatively lower amplitude and longer duration. A potential explanation for that could be the saturation effect of the sum of individual HRF. For example, if the amplitude of the estimated response saturates after summing over 6 HRFs then any stimulus lasting smaller than 6 TRs will have a relatively smaller amplitude than other stimuli which are longer than 6 TRs. Thus, one limitation that can be identified here is the low sensitivity of the approach in detecting short duration stimuli when present along with longer duration stimuli.

Preprints (www.preprints.org) | NOT PEER-REVIEWED | Posted: 15 September 2022 doi:10.20944/preprints202209.0217.v1

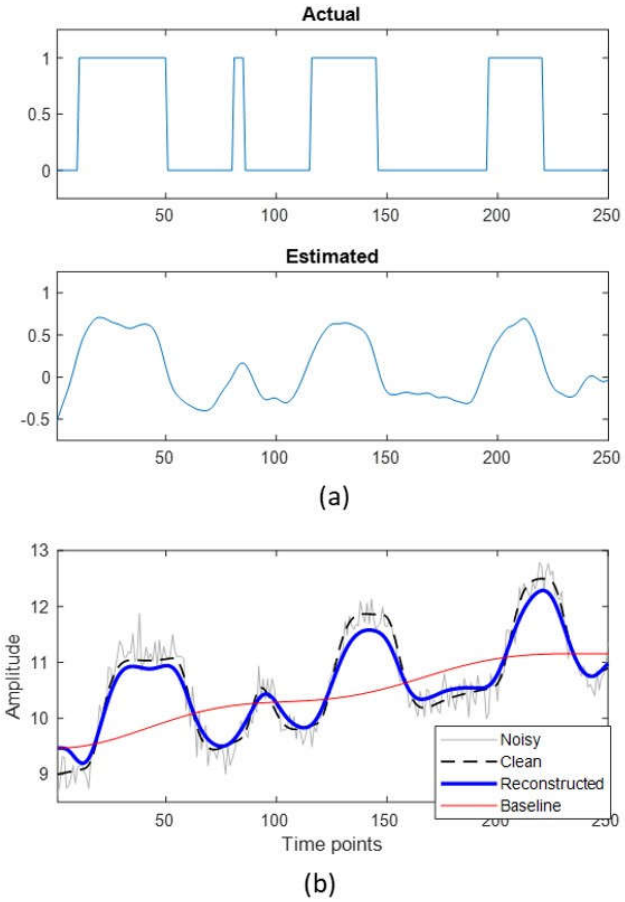

Figure 3. (a) The actual (top) and estimated (bottom) stimulus for a synthetic timeseries data. (b) synthetic time series. Noisy time series was obtained by adding gaussian noise and signal drift to the clean time series. The noisy time series was used as input for the proposed approach to obtain the estimated time series and estimated signal drift (baseline).

The proposed algorithm was used to estimate the pseudo-stimulus for all the voxels of the brain while performing a simple binary decision-making task. The estimated pseudo-stimulus for all the voxels can be visualized in form of a motion picture where each frame corresponds to a single time instance. The visualization of the pseudo stimulus for the brain responding to the app download decision is shown in Video 1. The animation shows the average response across all participants. The relative time is shown on top. The instance when the screenshot for a new app appears (beginning of new trial) is considered as T=0. The entire visualization if from 25 TRs (13.5 seconds) before the reference point to 25 TRs after the reference point. The 25 TRs after the reference point show the initial process of information gathering and early decision making. The 25 TRs before the reference point captures the events happening during the final decision-making process and the blanking period between two stimuli. The button press happens 5 seconds before the reference point. Thus, anything happening before that can be considered to be a part of the final decision-making task. The brain activity between the reference timepoint and 5 seconds before it indicates what happens after the end of stimulus during rest period. The pseudo-stimulus amplitude is normalized and converted to z-score. The amplitude corresponds to the strength of activation at any given time instance (estimated from the actual BOLD fMRI time series). The activation strength is corrected for the hemodynamic response delay and thus can be time locked with the experiment paradigm. From the animation a flow of brain activity can be observed in some of the regions, especially the visual cortex regions. The activity starts to peak with the onset of stimulus, it peaks for a while and then it drops below baseline for some time (deactivation) before reaching the

Preprints (www.preprints.org) | NOT PEER-REVIEWED | Posted: 15 September 2022 doi:10.20944/preprints202209.0217.v1

baseline again towards the end of resting period. Different brain regions being activated at the same time can be visualized simultaneously.

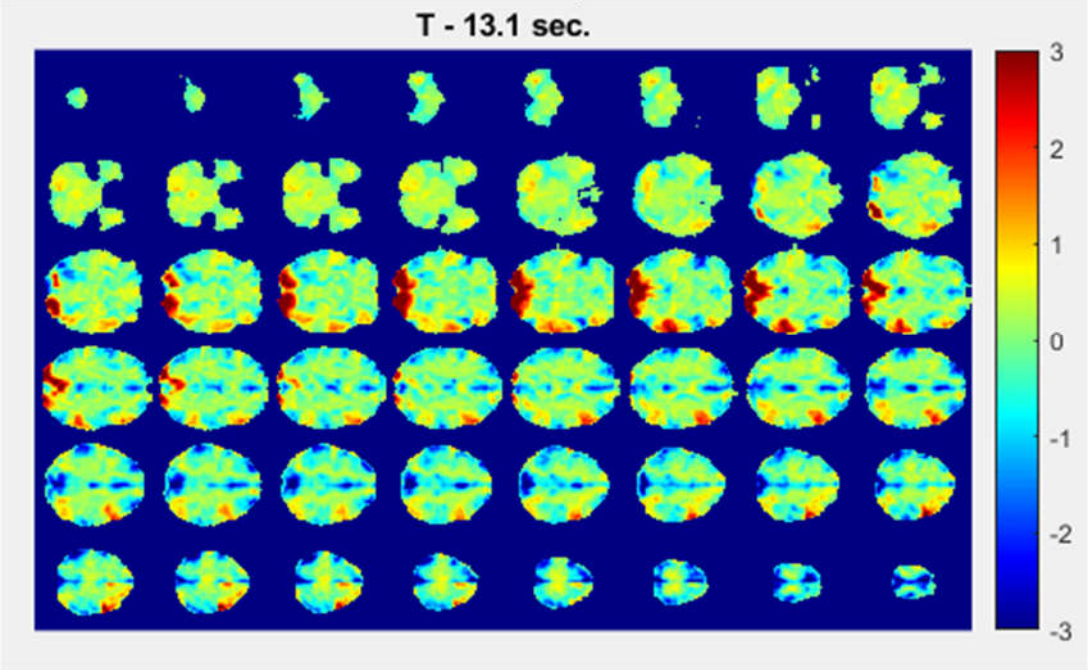

Video 1: Visualization of the pseudo-stimulus (normalized) across time. Different axial slices are visualized with Left hemisphere towards bottom and Right hemisphere towards top.

The temporal response for voxels in different brain regions is shown in Figure 4. At first the temporal response may seem very similar to the hemodynamic response obtained using the FIR modeling of the fMRI data [35] but there is a fundamental difference here. The hemodynamic response represents the response of the brain to a given stimulus. The hemodynamic response is obtained by averaging sections of the actual BOLD response and can be considered as the output of the brain to a stimulus. The temporal response or pseudo-stimulus on the other hand represents the perceived input to the brain (can be different for different regions). An experiment paradigm is usually considered as an input to the brain but not all brain regions respond to it at the same time. Some brain regions may receive an indirect input signal from other brain regions which directly respond to the external experiment paradigm. The input to such indirect regions would be different from the experiment paradigm. Thus, the input to all brain regions may not be the same and varying input to different parts of the brain is estimated in form of pseudo-stimulus or temporal response. By knowing the estimated input to different brain regions, it can be possible to identify at what time instance a given brain region was triggered. Apart from that, the hemodynamic response is convoluted with the HRF and is delayed by a few seconds w.r.t to actual stimulus [12] which is not the case with pseudo-stimulus. The algorithm corrects for HRF delays, and the temporal response can be time locked with the experiment paradigm providing a better temporal understanding of the dynamic processing of the brain.

Preprints (www.preprints.org) | NOT PEER-REVIEWED | Posted: 15 September 2022 doi:10.20944/preprints202209.0217.v1

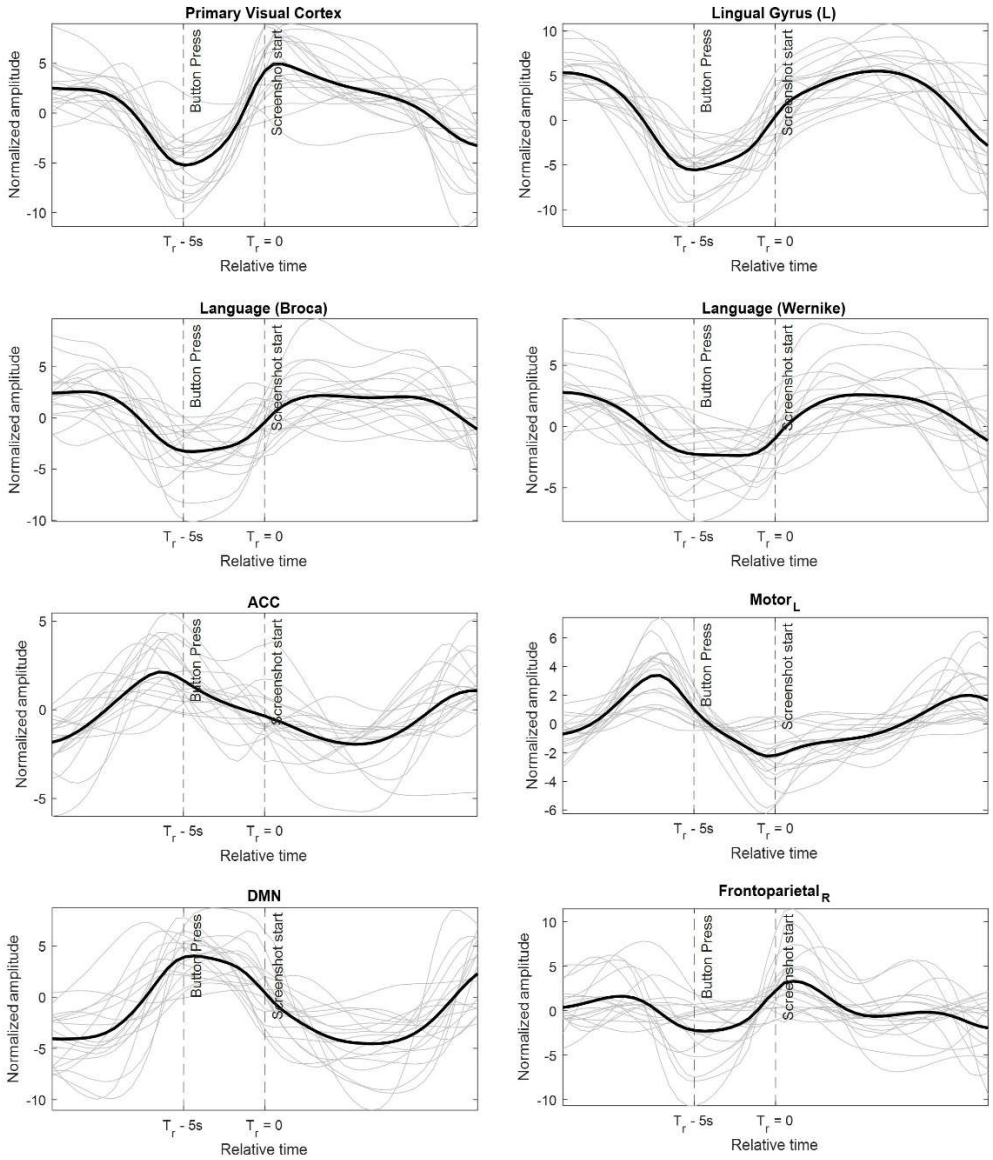

Figure 4. Estimated pseudo-stimulus (temporal response) for different voxels inside the brain. The plots in light grey corresponds to the temporal response from single subjects while the dark black plot is the average across all participants. The vertical dotted line indicates the time instance of button press and beginning of the stimulus.

Coming back to figure 4, the light-colored lines represent the response for each participant while the solid black line represents the averaged response. The temporal response is for all the apps irrespective of the download decision by the user. The time instance of button-press and the beginning of the stimulus is indicated with vertical dotted lines. The beginning of the stimulus initiates a strong activation in the visual cortex region. The visual cortex activation is caused due to the appearance of the screenshot and app description after the blank screen. The algorithm does correct for the hemodynamic response delays and thus the temporal response can be time locked to the experiment paradigm. Once the screenshot is displayed, the participants are likely to engage in the task of reading the description of the apps. The reading activity causes a gradual and prolonged activation of the Lingual gyrus which is involved in identification and recognition of words [36]. During the same time a prolonged activation is also observed in the Broca and the Wernike language regions. The activation of this region can be associated with semantic and syntactic interpretation of the app description [37, 38, 39]. Towards the end of the stimulus, decision independent activation is observed in the anterior cingulate cortex (ACC). ACC is shown to be involved in decision making tasks, especially outcome

Preprints (www.preprints.org) | NOT PEER-REVIEWED | Posted: 15 September 2022 doi:10.20944/preprints202209.0217.v1

evaluation before an actual decision is made [40, 41, 42]. Finally, a strong activation is observed in the left motor cortex just before the button press. Little to no activation is observed in the right motor cortex during the same time. The left motor cortex activation is presumably caused due to the finger movement with the right hand to indicate the download response.

Finally, during the blanking period between two stimuli, activation is observed in the default mode network. Default mode network has been shown to be a task negative brain region meaning it gets deactivated during the task and gets activated in the absence of any specific task [43]. An interesting temporal response is observed for the voxels within frontoparietal network. The temporal response shows a transient behavior where the activation peaks near button press and beginning of new stimulus. The transient behavior of the temporal response may indicate the involvement of the region in task switching. Previous studies have suggested the role of frontoparietal network as a flexibility hub [44] and in task switching [45]. The video 1 and figure 4 show the application of the proposed approach in extracting the dynamic spatial and temporal response to the app download decision making task.

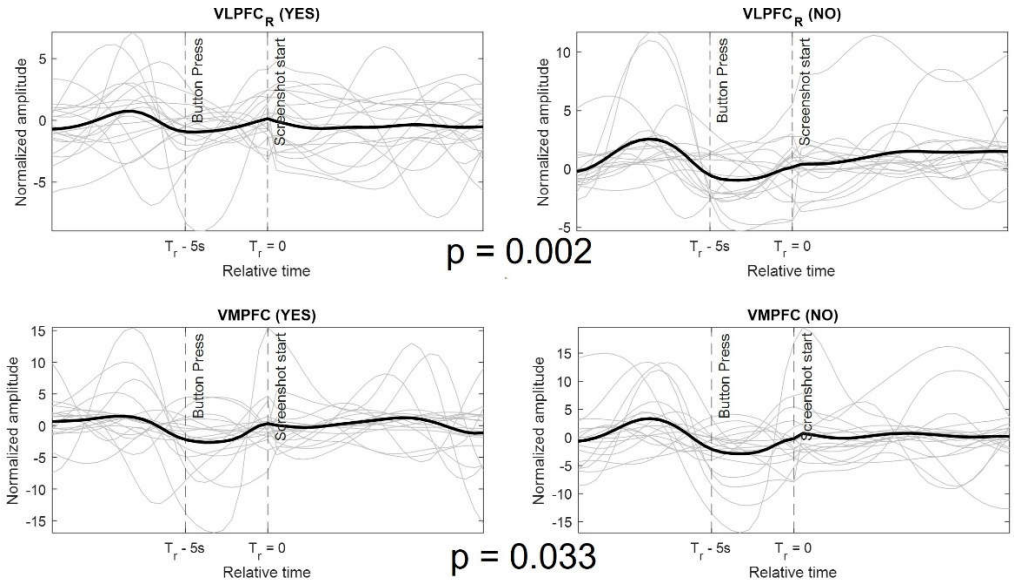

Figure 5. Difference in pseudo-stimulus for 'yes' (left column) and 'no' (right column) download decisions by the participants. The temporal response is shown for voxels in two regions that show a statistically significant difference between the 'yes' and 'no' apps. The p-values for the paired t test are shown between the subplots. The color coding of the plots is same as in Figure 4.

The temporal response from some of the brain regions depended on the user response for the apps. To identify the regions that responded differently for download and not download decision a paired t-test was performed. The algorithm extracts the pseudo stimulus for all the apps whose download decision was either 'yes' or 'no'. A paired t-test was performed on temporal response of each voxel and all participants. Only two brain region showed statistically significant difference in temporal response between 'yes' and 'no' response, the right ventrolateral prefrontal cortex (VLPFC) and the ventromedial prefrontal cortex (VMPFC). The VMPFC region has been shown to be involved in decision making involving reward [2, 46, 47]. Figure 5 shows the temporal response for the voxel showing the maximum difference in each region. The response is shown for both 'yes' and 'no' apps and for all participants. It can be observed from the figure that there is more activation for 'no' apps as compared to 'yes' apps, right before the final decision time.

Preprints (www.preprints.org) | NOT PEER-REVIEWED | Posted: 15 September 2022 doi:10.20944/preprints202209.0217.v1

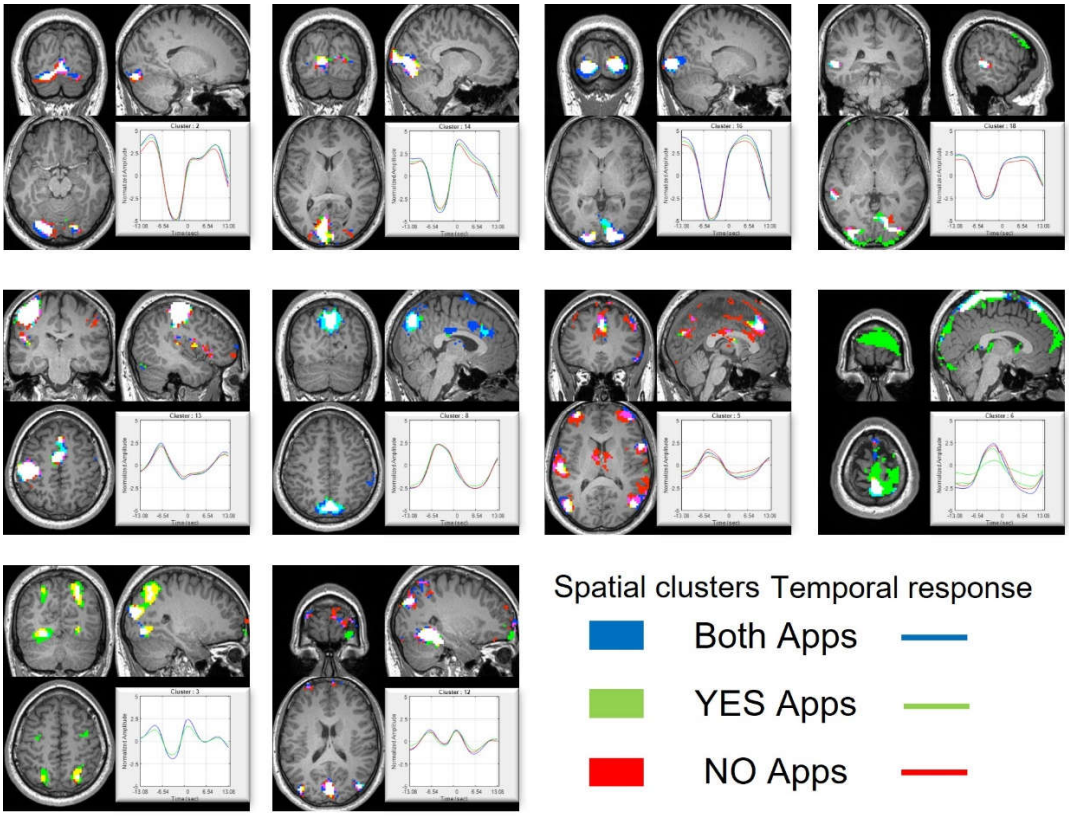

Figure 6: Spatial and temporal results for k-means clustering. Figure shows some of the clusters with meaningful temporal and spatial response. The response for 'yes' apps is shown in green, 'no' apps is shown in red and the case for all user decision (both yes and no) is shown in blue.

The k-means clustering results is summarized in Figure 6. The figure shows spatial clusters and the corresponding temporal response for the cluster. The cluster numbers are randomly assigned by the clustering algorithm and doesn't relate to the anything related to the stimulus. The cluster level temporal response is obtained from the centroids of the k-means. Temporal response and spatial parcellation for all the 20 clusters are shown in the appendix section. The color scheme corresponds to the user response to the apps. The pseudo-stimulus for all the voxels were extracted for 3 different cases. First for all the apps irrespective of their download decision, second, for all the apps where the user decided to download the apps and third, for all the apps where user decided not to download the app. The spatial cluster color and the time series color for each of the three cases are also shown in the figure. For spatial clusters, if there is an overlap in cluster for more than one cases (which was common) then the cluster color is obtained by mixing the individual colors. The k-means clustering was able to identify different brain regions based on their response to the stimuli. The activation peaks in the temporal response for different clusters corresponds to different stages in the decision-making task. The clustering approach was able to identify different brain regions in an unsupervised fashion. For example, clusters 14 and 16 corresponds to the visual cortex, cluster 2 corresponds to the lingual gyrus while cluster 18 contains the Broca and Wernicke language regions. All the above-mentioned clusters are active after the start of stimulus during the initial phase of information gathering.

Before the decision is made (indicated by a button press) activity peaks for clusters 5. Cluster 5 consists of spatial regions belonging to the executive control network, ACC, and dorsolateral prefrontal cortex (DLPFC). DLPFC has been shown to be active towards the end of the decision-making process [5, 9, 17]. Because of the similar temporal response, all the different spatial regions are grouped into a single cluster. Cluster 13 consists of the left motor cortex region while cluster 8 corresponds to the DMN. Motor cortex shows activity at the end of the stimulus while the DMN shows activity during the 5 second

 doi:10.20944/preprints202209.0217.v1

blanking period. Finally, the cluster 3 overlaps with the frontoparietal network and shows transient activity during the beginning and end of the main stimulus. The role of DMN and frontoparietal network have been discussed earlier. For clustering it is interesting to observe that even with an unsupervised clustering approach, it is possible to extract spatial regions with meaningful interpretations.

The proposed technique shows promising results in identification and visualization of the dynamic brain behavior. However, the algorithm is still in its early development stage and can be improved further. The results for a binary decision making task suggest that regularized deconvolution methods can be used to extract and visualize whole brain dynamic activation information from noisy fMRI data. There are some challenges that exist for effective operation of the proposed approach. First, there are a few hyper-parameters in the algorithm and the best combination of the hyper-parameters can still be explored. The set of hyperparameters used for obtaining the results shown in this paper were obtained from testing on synthetic and simulated data. The hyperparameter that has the maximum effect on the estimation of pseudo-stimulus is the regularization constant. Setting it too small may result in a noisy estimate while setting it too large may reduce the resolving ability for smaller stimuli. Some effects of the regularization constant for the closed form solution have been tested and described in the appendix section. Some of the earlier studies have shown SNR based regularized constant value selection techniques, mainly targeted for iterative L1 regularization [Uruñuela et al., 2021].

As discussed earlier, another limitation is the inability to fully resolve smaller (short time) stimuli due to the saturation effect. Because of its sparse nature, L1 regularization approach may provide superior results for identification of neuronal activation in an event related experiment design. One more limitation lies in the selection of the HRF. It has been tested that, small variations in amplitude and time shifting doesn't have a large-scale effect on the estimation of the pseudo-stimulus. The details of the HRF variability have been discussed in the appendix section. However, a large variation in the HRF may result in inaccurate results. Another possible future work can be to use and check the effects of regions specific HRF models for estimation of the pseudo-stimulus.

4. Conclusion

The main objective of this paper is to present a technique that can be used to estimate and visualize the dynamic nature of whole brain activity. The proposed technique is based on the linear deconvolution model. The technique was applied to a simple binary decision-making task and various regions involved in the decision-making process were identified. The focus was more on the approach itself rather than the decision-making inferences and thus the discussion about the neurological interpretation is limited. However, a detailed analysis was conducted on the algorithm itself. From the results, it can be shown that the proposed algorithm is capable of extracting the region level stimuli as seen by the brain. The so-called pseudo-stimuli is also visualized in form of a motion picture which clearly shows the dynamic brain activity across whole brain. Along with that, with a little post processing, meaningful spatial clusters can also be obtained in an unsupervised manner by using the extracted pseudo stimuli. There are many aspects of the algorithm that can be improved but the identification of whole brain activity information can be very useful for future research and in better understanding the dynamic process happening inside the brain during various tasks.

Author Contributions: Conceptualization, Harshit Parmar; Data curation, Harshit Parmar; Funding acquisition, Eric Walden; Methodology, Harshit Parmar; Project administration, Eric Walden; Resources, Eric Walden; Software, Harshit Parmar; Validation, Eric Walden; Visualization, Harshit Parmar; Writing – original draft, Harshit Parmar; Writing – review & editing, Eric Walden.

Funding: This research received no external funding.

Institutional Review Board Statement: Written consent was obtained from all the participants prior to commencing the experiment. All the participants were also screened for MRI safety with a

 doi:10.20944/preprints202209.0217.v1

separate MRI safety screening form. This study was approved by the Texas Tech Human Research Protection Program with number IRB2016-557.

Informed Consent Statement: Informed consent was obtained from all subjects involved in the study

Data Availability Statement: The datasets generated for this study and the MATLAB codes used for the analysis of the data are available on request to the corresponding author. Requests to access these datasets should be directed to HP, harshit.parmar@ttu.edu.

Acknowledgments: We would like to thank Kasey Rieken for assisting with the data collection process.

Conflicts of Interest: The authors declare that the research was conducted in the absence of any commercial or financial relationships that could be construed as a potential conflict of interest.

Appendix A: Synthetic Data with Varying Noise

The effect of noise was tested on the estimation of the pseudo stimulus using synthetic single time series data. For a given experiment paradigm, multiple time series were generated using different noise variance. For each case, the pseudo stimulus was estimated using the proposed algorithm. All the parameters of the algorithm were kept same. Figure A1 (on the right) shows the estimated pseudo stimulus for varying noise levels. The correlation between the actual experiment paradigm and the pseudo stimulus is also displayed in the top right corner of each subplot. Figure also shows (on the left) the actual noisy time series and reconstructed time series along with baseline for varying noise scenarios. A total of 5 different noise levels were tested where the signal to noise ratios (SNR) were SNR = {10, 4, 2, 1, 0.5}. The accuracy of the estimated pseudo stimulus decreases with increasing noise level which can be directly observed in decreasing values of the correlation between the estimated and the actual stimulus with increasing noise.

Appendix B: The Effect of Regularization Constant

In terms of linear systems analysis, the process of extracting the pseudo stimulus from the observed BOLD signal is a simple deconvolution problem. However, because of the presence of noise, simple deconvolution is not very effective. Hence a regularized deconvolution approach is preferred here. The main advantage of the proposed approach is the ability to detect the pseudo stimulus even from a noise BOLD time series. Regularization plays a major role in estimating the pseudo stimulus. The effect of regularization is also tested for the proposed algorithm. Figure A2 demonstrates the effect of regularization on the extraction of pseudo stimulus. A total of 5 different regularization constant values were tested ($\lambda = \{5 \times 10^{-1}, 5 \times 10^{-2}, 5 \times 10^{-3}, 5 \times 10^{-4}, 5 \times 10^{-5}\}$). From the figure it can be observed that for very small values of regularization, the effect of noise is significant, and the extracted pseudo stimulus is not meaningful. On the other hand, for very large values of regularization constant, even useful signal has been treated as noise and only the very dominant effects in the experiment design are extracted. The reconstructed signal is also not anything like the noisy or the clean BOLD signal. Thus, too much or too little regularization is of no use, which is also supported by the correlation values between actual and estimated pseudo stimulus. Taking reference from the simulated data, the regularization constant for the entire algorithm was chosen to be 1×10^{-2}.

Preprints (www.preprints.org) | NOT PEER-REVIEWED | Posted: 15 September 2022 doi:10.20944/preprints202209.0217.v1

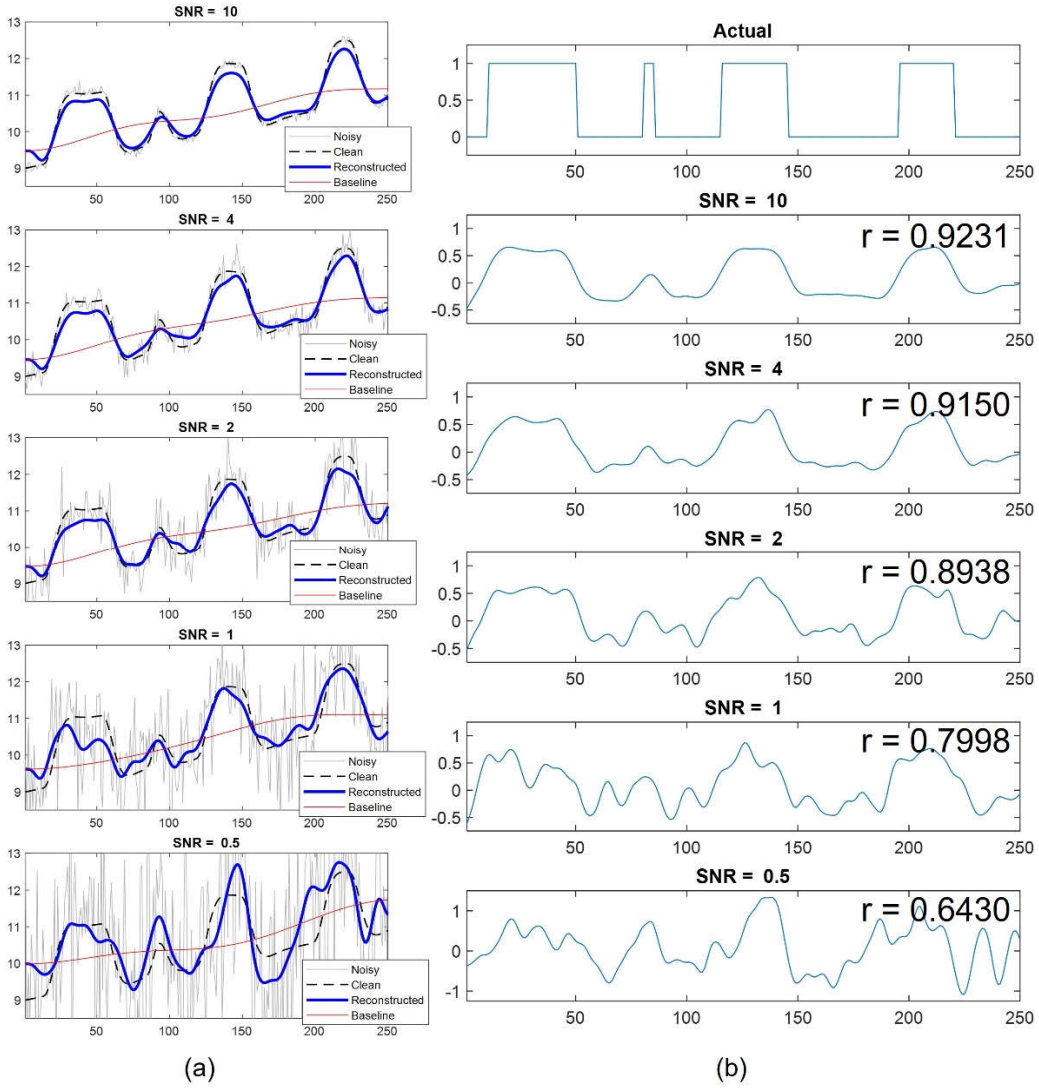

Figure A1: Comparison of the (left) time series reconstruction and (right) estimated pseudo stimulus for different noise levels. Varying noise levels are indicated using signal-to-noise ratio (SNR).

Appendix C: The Effect of HRF Variability

One of the assumptions made in the algorithm is the model for hemodynamic response function. The canonical double gamma HRF is used in estimation of the pseudo stimulus. However, it has been shown in previous studies that there is a variability in the HRF function from individual to individual. The effect of HRF variability was also checked for the proposed algorithm. To check the effect of HRF variability, the synthetic time series was generated using a different HRF than used in the algorithm. The results for HRF variability are shown in figure A3. As shown in subplot (a), the synthetic time series was generated using the original HRF model shown in blue. Two separate HRF model were then used independently to estimate the pseudo stimulus. The variation in the HRF includes difference in peak amplitude, time to peak and full width half maxima (FWHM). Subplot (c) and (d) shows the original and reconstructed time series for both the HRF models. Subplot (b) shows the extracted pseudo-stimulus using different HRFs. The correlation between the pseudo stimulus and the actual experiment stimulus is also shown in the subplot.

Preprints (www.preprints.org) | NOT PEER-REVIEWED | Posted: 15 September 2022 doi:10.20944/preprints202209.0217.v1

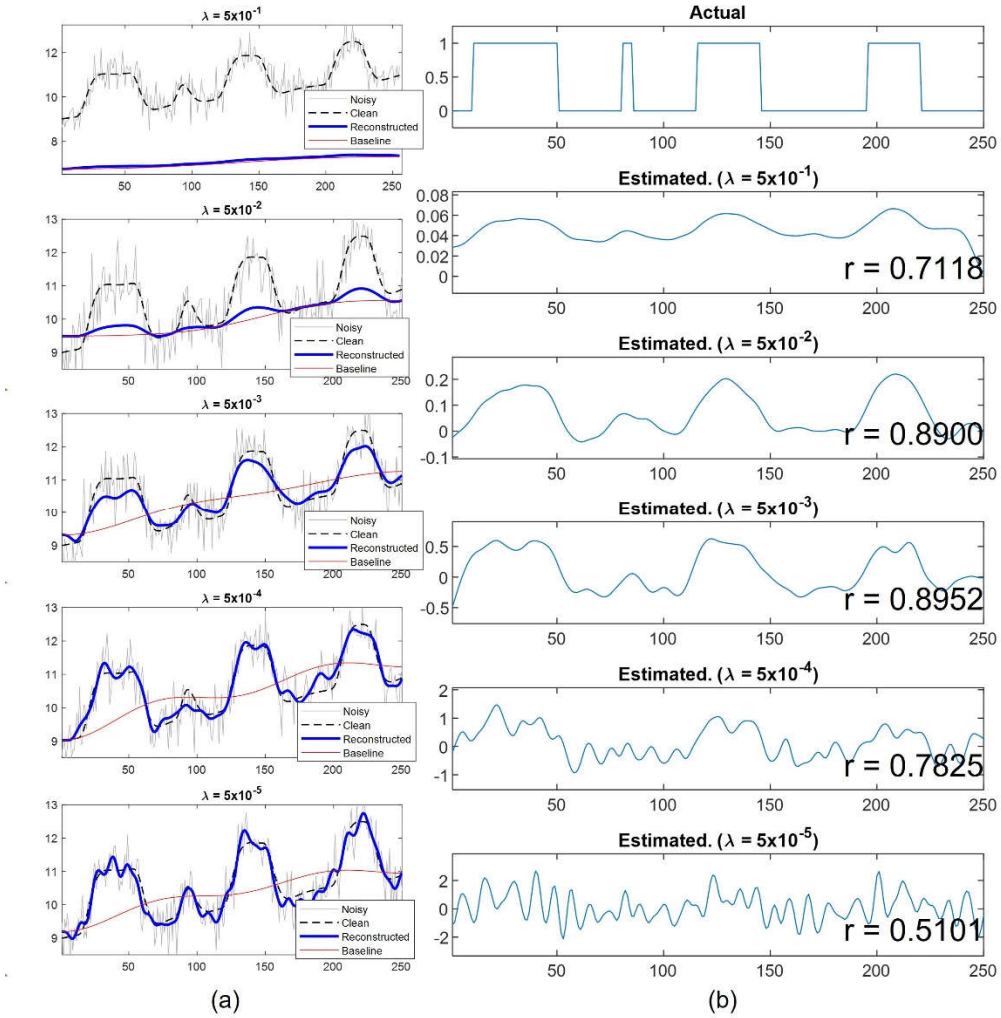

Figure A2: Comparison of the (left) time series reconstruction and (right) estimated pseudo stimulus for different regularization constant. Varying regularization constant values are indicated on the top of the subplots.

It can be observed from subplot (b) that the variation in amplitude has no significant difference in the extracted pseudo stimulus. However, the difference in peak time does have some effect. Depending on the difference in the peak time, the extracted pseudo stimulus appears to be either forward or reverse time shifted. The amount of time shift is equal to the difference in the two HRF model. The HRF model with larger FWHM extracts smoother (less high frequency components) pseudo-stimulus. For large FWHM, the overlap between adjacent HRF in the design matrix is more as compared to shorted FWHM and thus the extracted pseudo stimulus appears smoother. Overall, the correlation of the extracted pseudo stimulus with the actual experiment stimulus is high and useful information can be extracted from both the cases.

Preprints (www.preprints.org) | NOT PEER-REVIEWED | Posted: 15 September 2022 doi:10.20944/preprints202209.0217.v1

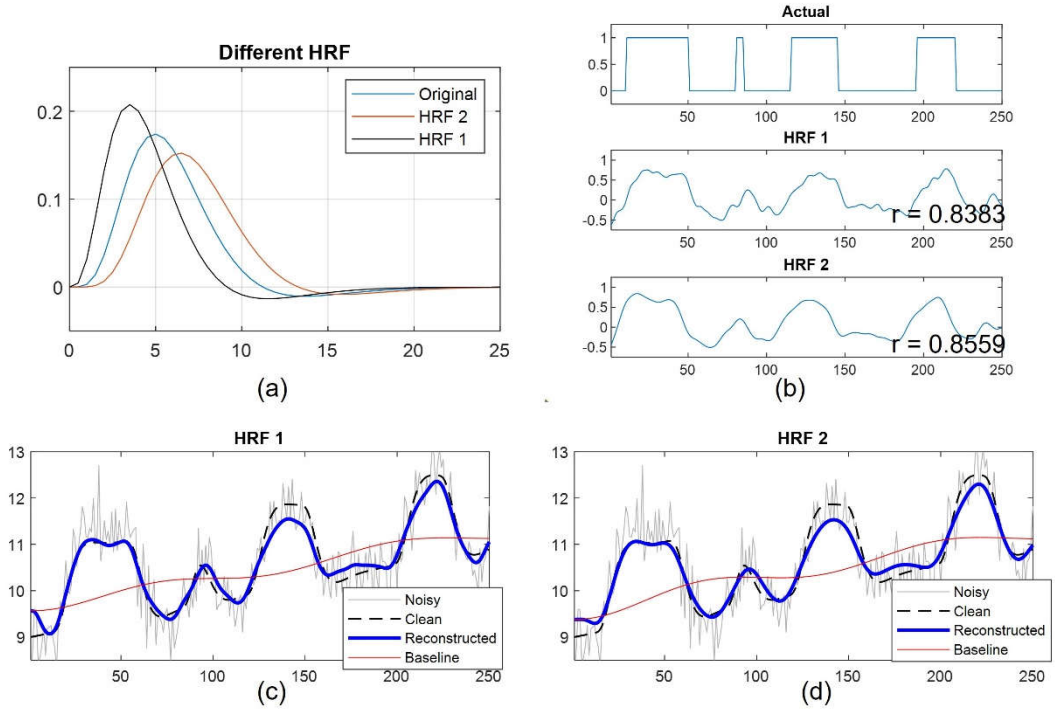

Figure A3: Checking the effect of HRF variability. (a) Different HRF models. (b) Estimated pseudo stimulus using different HRF models. The correlation between the pseudo stimulus and the actual experiment design is also shown in the subplot. (c & d) Original and reconstructed time series obtained using different HRF models.

Appendix D: K-means Clusters

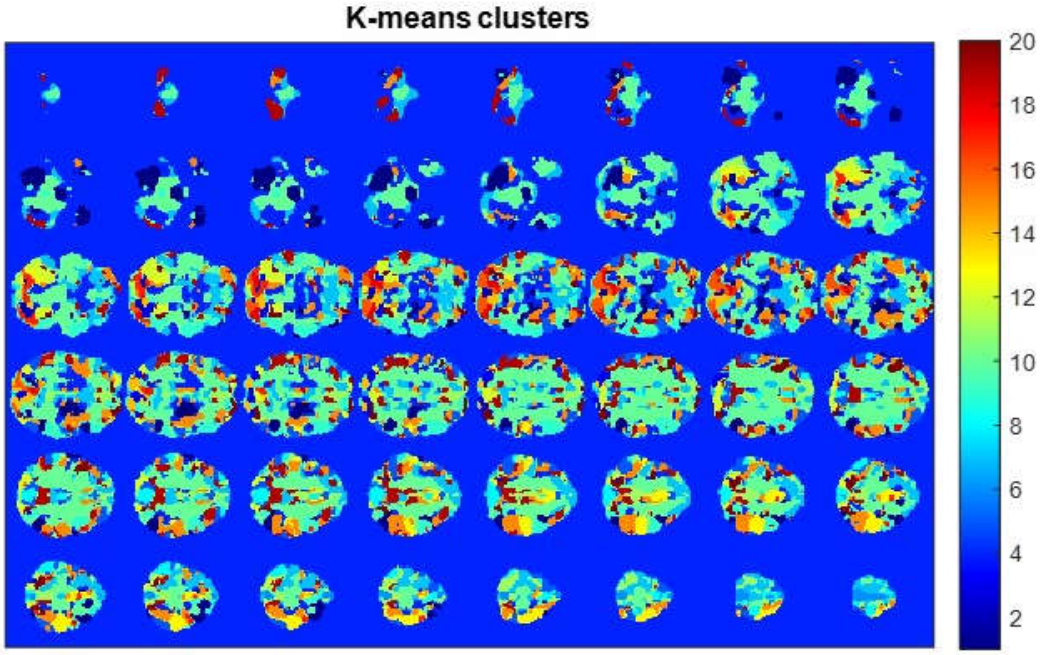

Figure A4: Spatial clusters obtained after k-means clustering. The clusters are color coded, and the color bar represents the color corresponding to cluster numbers.

The spatial clusters and the corresponding time series for all 20 clusters is shown in figures A4 and A5 respectively. The spatial clusters are shown for all the apps (irrespective of the response) while the representative time series for all the clusters is shown for all 3

Preprints (www.preprints.org) | NOT PEER-REVIEWED | Posted: 15 September 2022 doi:10.20944/preprints202209.0217.v1

cases (irrespective of the response, only yes response and only no response to download decision).

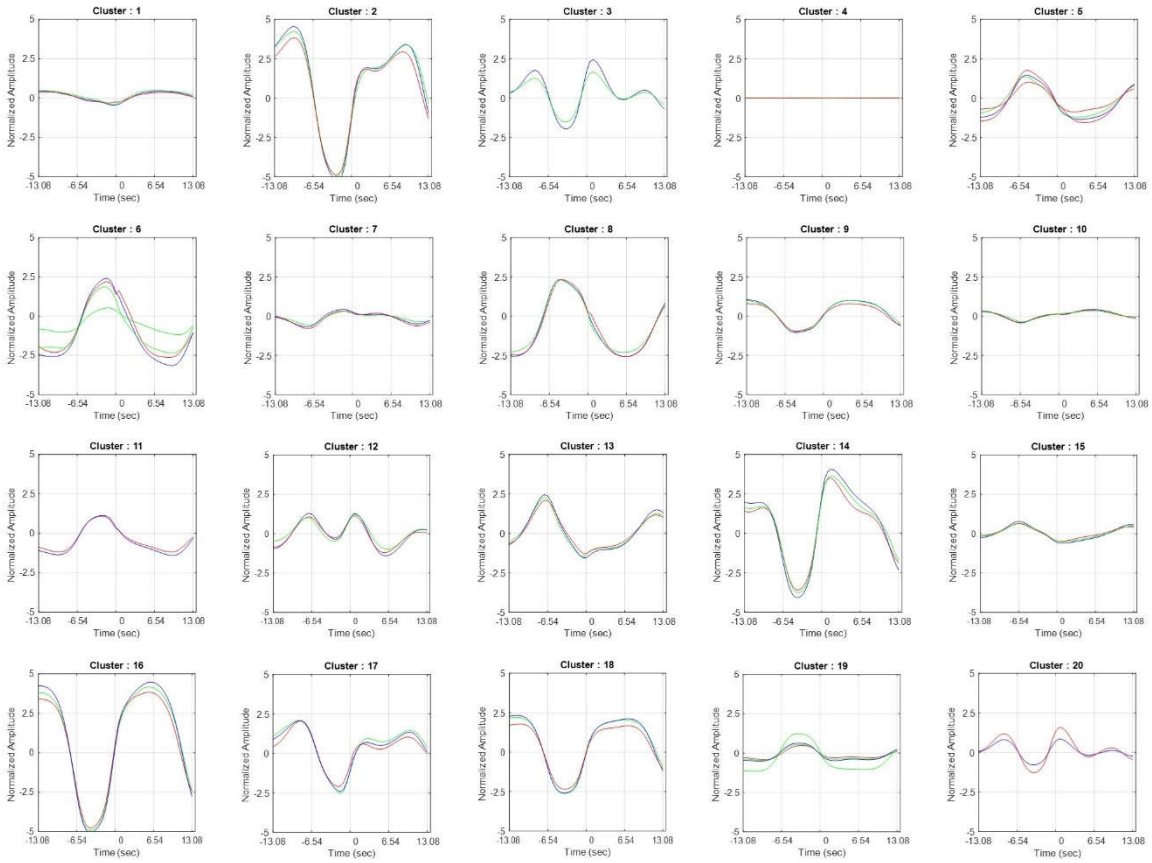

Figure A5: Temporal for each of the 20 spatial cluster shown in figure A4. The response for 'yes' apps is shown in green, 'no' apps is shown in red and the case for all user decision (both yes and no) is shown in blue. The x-axis represents normalized time that is centered at the beginning of new app (new stimulus) while the y-axis represents averaged normalized amplitude.

Appendix E: Effect of λ

One of the important parameters for regularized linear deconvolution is the regularization constant 'λ'. Often a different value of λ is used for each voxel due to different SNR (signal to noise ratio). Moreover, for L1 regularization, the value of λ is updated after every iteration. The effect of λ on the estimation of pseudo stimulus was tested using synthetic data. Synthetic time series with varying noise level was generated. The pseudo stimulus was estimated using different values of λ and a correlation was computed between the actual experiment design and the estimated pseudo stimulus. The plots of λ vs correlation for different SNR is shown in figure A6. Section (a) and (b) of figure A6 shows the results for 2 different time series. In each section, the top subplots show the ground truth and the noisy (observed) time series for different SNR. The bottom subplots show the change in correlation between the actual and estimated (pseudo stimulus) experiment design as a function of λ. It can be observed from the figure that there is a range of λ values for which the correlation between the actual and estimated experiment design remains almost constant (high correlation value plateau region). The range of λ becomes smaller with decreasing SNR but for a certain range of λ values, a high correlation is observed irrespective of the SNR or time series type. The simulation results suggest that as long as a constant λ value is selected within the plateau region, the estimated pseudo stimulus would be accurate irrespective of the absolute SNR of the voxel's time series. Thus, a

Preprints (www.preprints.org) | NOT PEER-REVIEWED | Posted: 15 September 2022 doi:10.20944/preprints202209.0217.v1

constant λ value was used for analysis. Moreover, having a constant λ value reduces the computational complexity and computation time.

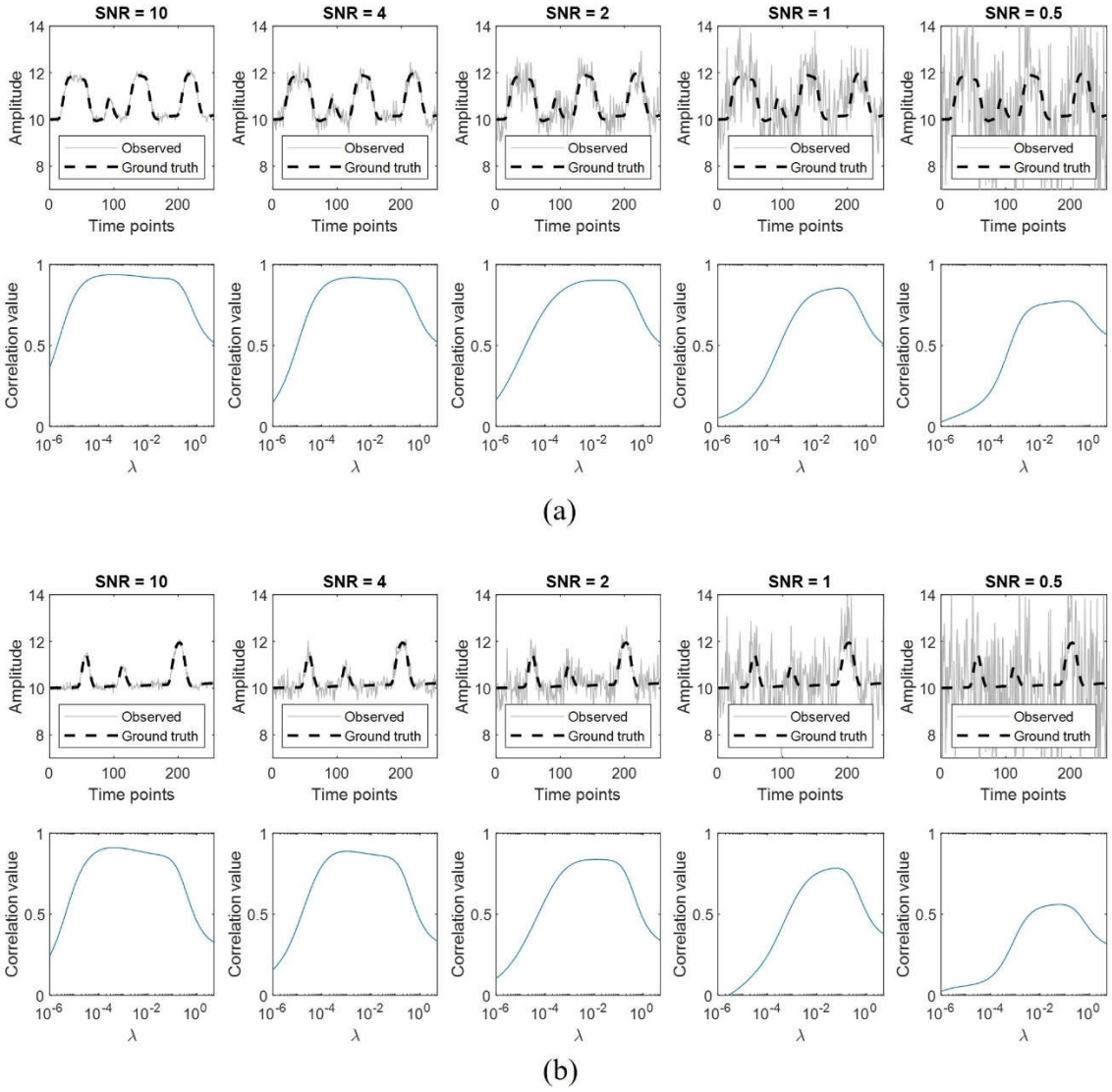

Figure A6: Effect of regularization constant (λ) on estimation of pseudo stimulus. Results shown for varying SNR for two different types of synthetic data (a) and (b). Each column represents results for a different SNR indicated above the top subplot. The top subplot shows the ground truth and the noise time series. The bottom subplot represents the correlation between actual (ground truth) and estimated (pseudo stimulus) as a function of λ.

Appendix F: L1 regularization of first difference

The first difference of the ground truth (experiment design) has a sparse nature. Thus, a different regularization function was also tested. Equation A1 below shows the loss function which consists of 2 parts. The first part, E(w) (equation A2), is the error between the actual and the predicted response while the second part, R(w) (equationA3), describes the new regularization function. This regularization function is the L1 norm of the first difference of the weight vector. The gradient for the regularization function, which is derived in appendix G, is given in equation A4. The new regularization function was first tested on synthetic data with different SNR and then applied to real fMRI data.

Preprints (www.preprints.org) | NOT PEER-REVIEWED | Posted: 15 September 2022 doi:10.20944/preprints202209.0217.v1

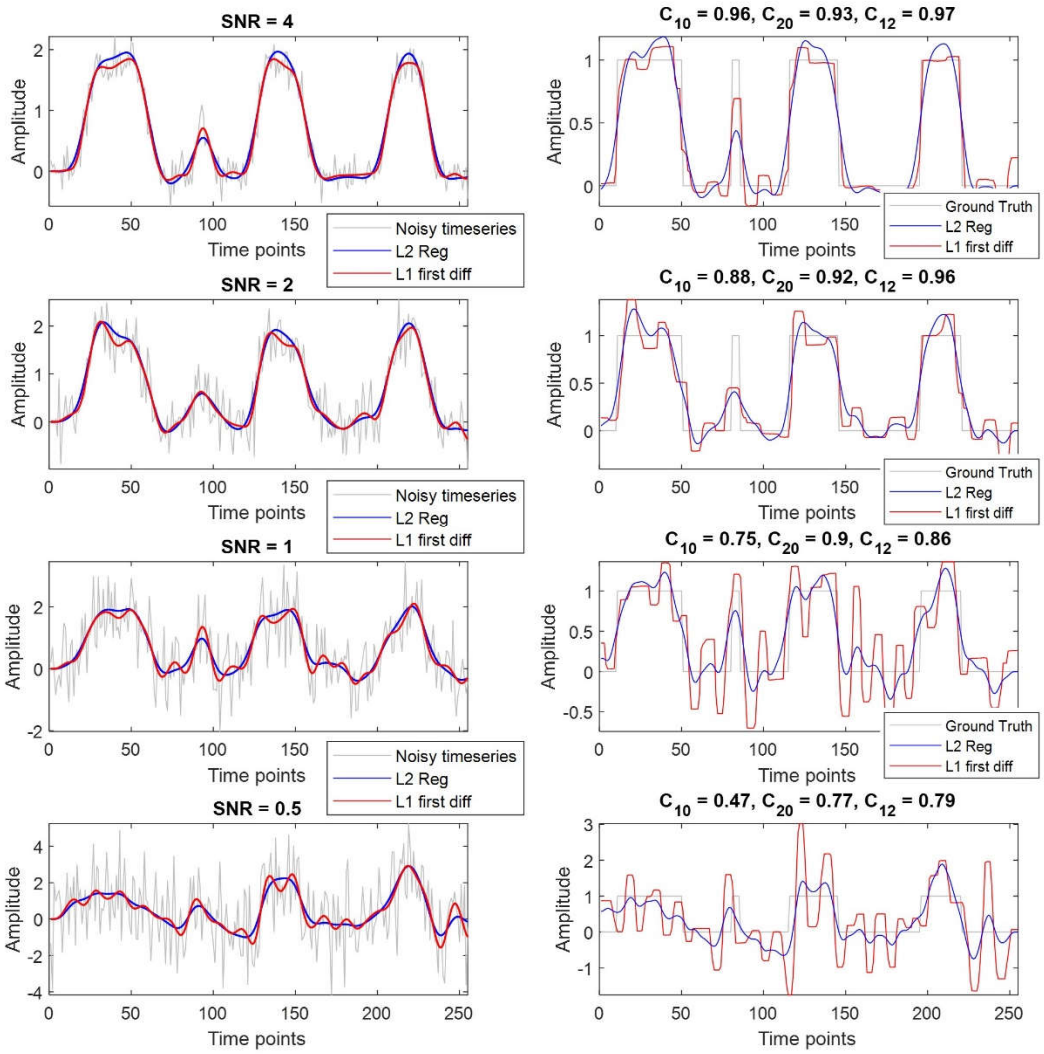

Figure A7: Comparison of L1 of the first difference and L2 regularization on synthetic time series data. Left column subplot shows synthetic noisy time series (grey) with reconstruction using different regularization shown in red (L1 first difference) and blue (L2). Right column subplots show ground truth experiment design (grey) with estimated pseudo stimulus using different regularization shown in red (L1 first difference) and blue (L2). Each row subplot corresponds to a different SNR value indicated in the title of the left subplots.

$$L(w) = E(w) + R(w)$$

Equation A1

$$E(w) = \frac{1}{2N}\sum_{n=1}^{N}\left(\hat{Y}_n - Y_n\right)^2$$

Equation A2

$$R(w) = \lambda \sum_{k=1}^{T-1} |w_{k+1} - w_k|$$

Equation A3

Preprints (www.preprints.org) | NOT PEER-REVIEWED | Posted: 15 September 2022 doi:10.20944/preprints202209.0217.v1

$$\frac{\partial R(w)}{\partial w_k} = \lambda \left(\frac{w_k - w_{k+1}}{|w_{k+1} - w_k|} + \frac{w_k - w_{k-1}}{|w_k - w_{k-1}|} \right)$$

Equation A4

Figure A7 shows results of the new regularization function on synthetic data. The left column shows the noisy time series (grey) and the reconstructed time series for L2 regularization (blue) and the L1 regularization of the first difference of w (red). The right column shows the ground truth (grey) and the estimated pseudo stimulus using L2 regularization (blue) and the L1 regularization of the first difference of w (red). Each row corresponds to the synthetic data with different SNR, as indicated on top of the left subplots. It can be observed that the estimated pseudo stimulus for L1 of first difference and L2 regularization both are very similar in nature. Due to sparse nature of L1 regularization, the pseudo stimulus appears more rectangular in shape. Both the estimated pseudo stimuli show high correlation with the ground truth. Pearson correlation coefficient was computed between the ground truth and the estimated pseudo stimulus using both the approach. In the figure, C10 indicates the correlation between the ground truth and pseudo stimulus obtained using L1 regularization of the first difference, C20 indicates the correlation between the ground truth and pseudo stimulus obtained using L2 regularization, while C12 indicates the correlation between the pseudo stimulus obtained using L1 regularization of the first difference and L2 regularization. The correlation values suggest that L2 regularization performs slightly better than the L1 regularization of the first difference. The performance of the L1 regularization degrades more with decrease in SNR as compared to L2 regularization.

The group level spatial and temporal results for L1 regularization of the first difference is shown in Figure A8. The solution to the optimization using L1 regularization of the first difference was solved by an iterative process. As discussed in appendix G, a modified pipeline was used to obtain group level results. The group level results are very similar to the results obtained using L2 regularization. The temporal smoothing of the pseudo stimulus may be caused by the averaging of response across all the trials and participants. The positive and negative peaks time locked to the experiment design is observed. The spatial clusters 2 and 3 overlap with the visual cortex regions and the temporal response shows a positive peak at the beginning of the trial. The clusters 19 and 20 overlap with the default mode network and their temporal response peaks during the blanking period (between the button press and beginning of the new trial). As discussed earlier, default mode network is a task negative network, and the temporal response for clusters 19 and 20 seems to be following that trend. Spatial cluster 13 overlaps with the brain regions of DLPFC, VMPFC and ACC. The temporal response for cluster 13 peaks towards the end of the decision-making process, which is similar to results observed for L2 regularization and discussed in section 3 above. The motor cortex overlaps with cluster 7 and the temporal response has a dominant peak towards the end of the trial as observed for results of L2 regularization.

However, the main limitation of iterative approach is the computation time required for voxel wise full brain analysis. A timing analysis was performed on synthetic data. To estimate the pseudo stimulus using an iterative approach on a synthetic time series of 2048 time points, takes on an average (averaged over 20 runs) slightly more than 5 seconds for 1000 iterations. Convergence was achieved between 1000 and 2000 iterations. Assuming about 60,000 voxels within the brain region for a 3mm x 3mm x 3mm resolution volume, the total time required to perform voxel-wise analysis for a single subject would be 300,000 seconds (60,000 x 5) or about 83 hours. For a group of 20 participants that would be more than 2 months. A reduction in time can be achieved by using parallel processing and high-performance computing centers but still the time required to perform voxel-wise analysis would be much higher for iterative approach as compared to L2 regularization with closed for solution, which only takes few minutes to couple of hours for a single

Preprints (www.preprints.org) | NOT PEER-REVIEWED | Posted: 15 September 2022 doi:10.20944/preprints202209.0217.v1

participant. Thus, if similar results are obtained, it is much more practical to use the faster L2 regularization over other iterative regularization approaches.

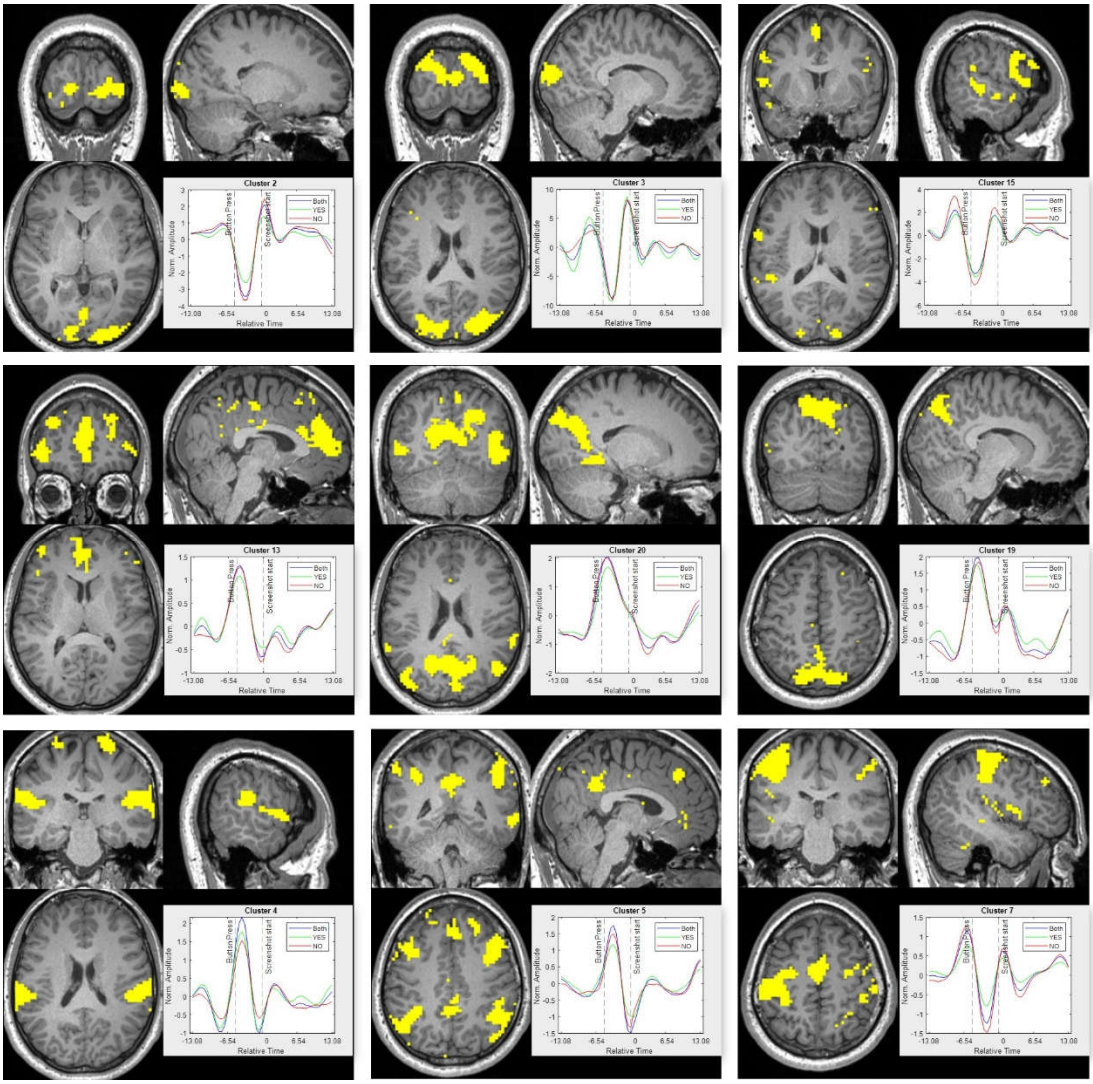

Figure A8: Spatial and temporal results for L1 regularization of the first difference. The spatial maps correspond to k-means clusters. The cluster numbers are indicated on top of the time series subplot. The temporal plot shows the mean response of the clusters to 'YES' apps (green), 'NO' apps (red) and 'all' apps (blue). The temporal response is centered at the beginning of the new trial. The instance of button press and beginning of new trial is indicated with dotted lines.

Appendix G: Gradient computation for R(w)

This section derives the gradient of the regularization loss function for L1 regularization of the first difference. The regularization loss function is shown in equation A5. The computed gradient for the weight for the kth time point is shown in equation A10. Because the gradient requires the weight from the previous and next time point, equation A10 is only valid for 1< k < T. For the values of 'k' outside the range, we assume wk to be zero. Corresponding to that the gradient for the weights for the first and the last time point is shown in equations A11 and A12 respectively.

$$R(w) = \lambda \sum_{k=1}^{T-1} |w_{k+1} - w_k|$$

Equation A5

Preprints (www.preprints.org) | NOT PEER-REVIEWED | Posted: 15 September 2022 doi:10.20944/preprints202209.0217.v1

$$R(w) = \lambda \sum_{k=1}^{T-1} \sqrt{(w_{k+1} - w_k)^2}$$

Equation A6

$$R(w) = \lambda \sum_{k=1}^{T-1} \sqrt{({w_{k+1}}^2 + {w_k}^2 - 2w_{k+1}w_k)}$$

Equation A7

$$\frac{\partial R(w)}{\partial w_k} = \lambda \frac{\partial}{\partial w_k} \left(\sqrt{({w_{k+1}}^2 + {w_k}^2 - 2w_{k+1}w_k)} + \sqrt{({w_k}^2 + {w_{k-1}}^2 - 2w_k w_{k-1})} \right)$$

Equation A8

$$\frac{\partial R(w)}{\partial w_k} = \lambda \left[\frac{1}{2}(2w_k - 2w_{k+1})({w_{k+1}}^2 + {w_k}^2 - 2w_{k+1}w_k)^{-\frac{1}{2}} + \frac{1}{2}(2w_k - 2w_{k-1})({w_k}^2 + {w_{k-1}}^2 - 2w_k w_{k-1})^{-\frac{1}{2}} \right]$$

Equation A9

$$\frac{\partial R(w)}{\partial w_k} = \lambda \left(\frac{w_k - w_{k+1}}{|w_{k+1} - w_k|} + \frac{w_k - w_{k-1}}{|w_k - w_{k-1}|} \right); 1 < k < T$$

Equation A10

$$\frac{\partial R(w)}{\partial w_1} = \lambda \left(\frac{w_1 - w_2}{|w_1 - w_2|} + 1 \right)$$

Equation A11

$$\frac{\partial R(w)}{\partial w_T} = \lambda \left(1 + \frac{w_T - w_{T-1}}{|w_T - w_{T-1}|} \right)$$

Equation A12

References

1. Forbes, Erika E., J. Christopher May, Greg J. Siegle, Cecile D. Ladouceur, Neal D. Ryan, Cameron S. Carter, Boris Birmaher, David A. Axelson, and Ronald E. Dahl. "Reward-related decision-making in pediatric major depressive disorder: an fMRI study." Journal of Child Psychology and Psychiatry 47, no. 10 (2006): 1031-1040.
2. O'Doherty, John P., Alan Hampton, and Hackjin Kim. "Model-based fMRI and its application to reward learning and decision making." Annals of the New York Academy of sciences 1104, no. 1 (2007): 35-53.
3. Hewig, Johannes, Thomas Straube, Ralf H. Trippe, Nora Kretschmer, Holger Hecht, Michael GH Coles, and Wolfgang HR Miltner. "Decision-making under risk: an fMRI study." Journal of Cognitive Neuroscience 21, no. 8 (2009): 1642-1652.
4. Cservenka, Anita, and Bonnie J. Nagel. "Risky decision-making: An fMRI study of youth at high risk for alcoholism." Alcoholism: Clinical and Experimental Research 36, no. 4 (2012): 604-615.
5. Laureiro-Martínez, Daniella, Stefano Brusoni, Nicola Canessa, and Maurizio Zollo. "Understanding the exploration–exploitation dilemma: An fMRI study of attention control and decision-making performance." Strategic management journal 36, no. 3 (2015): 319-338.
6. Vatansever, Deniz, David K. Menon, and Emmanuel A. Stamatakis. "Default mode contributions to automated information processing." Proceedings of the National Academy of Sciences 114, no. 48 (2017): 12821-12826.
7. Heekeren, Hauke R., Isabell Wartenburger, Helge Schmidt, Hans-Peter Schwintowski, and Arno Villringer. "An fMRI study of simple ethical decision-making." Neuroreport 14, no. 9 (2003): 1215-1219.
8. Schaich Borg, Jana, Catherine Hynes, John Van Horn, Scott Grafton, and Walter Sinnott-Armstrong. "Consequences, action, and intention as factors in moral judgments: An fMRI investigation." Journal of cognitive neuroscience 18, no. 5 (2006): 803-817.
9. Rosenbloom, Michael H., Jeremy D. Schmahmann, and Bruce H. Price. "The functional neuroanatomy of decision-making." The Journal of neuropsychiatry and clinical neurosciences 24, no. 3 (2012): 266-277.
10. Bandettini, Peter A., Eric C. Wong, R. Scott Hinks, Ronald S. Tikofsky, and James S. Hyde. "Time course EPI of human brain function during task activation." Magnetic resonance in medicine 25, no. 2 (1992): 390-397.
11. Ogawa, Seiji, Tso-Ming Lee, Asha S. Nayak, and Paul Glynn. "Oxygenation-sensitive contrast in magnetic resonance image of rodent brain at high magnetic fields." Magnetic resonance in medicine 14, no. 1 (1990): 68-78.

12. Handwerker, Daniel A., John M. Ollinger, and Mark D'Esposito. "Variation of BOLD hemodynamic responses across subjects and brain regions and their effects on statistical analyses." Neuroimage 21, no. 4 (2004): 1639-1651.
13. Handwerker, Daniel A., Javier Gonzalez-Castillo, Mark D'esposito, and Peter A. Bandettini. "The continuing challenge of understanding and modeling hemodynamic variation in fMRI." Neuroimage 62, no. 2 (2012): 1017-1023.
14. Krüger, Gunnar, and Gary H. Glover. "Physiological noise in oxygenation-sensitive magnetic resonance imaging." Magnetic resonance in medicine 46, no. 4 (2001): 631-637.
15. Lindquist, M. A. (2008). The statistical analysis of fMRI data. Statistical science, 23(4), 439-464.
16. Friston, Karl J., Peter Jezzard, and Robert Turner. "Analysis of functional MRI time-series." Human brain mapping 1, no. 2 (1994): 153-171.
17. Fellows, Lesley K. "The cognitive neuroscience of human decision making: a review and conceptual framework." Behavioral and cognitive neuroscience reviews 3, no. 3 (2004): 159-172.
18. Glover, Gary H. "Deconvolution of impulse response in event-related BOLD fMRI1." Neuroimage 9, no. 4 (1999): 416-429.
19. Makni, Salima, Philippe Ciuciu, Jérôme Idier, and J-B. Poline. "Semi-blind deconvolution of neural impulse response in fMRI using a Gibbs sampling method." In 2004 IEEE International Conference on Acoustics, Speech, and Signal Processing, vol. 5, pp. V-601. IEEE, 2004.
20. Cherkaoui, Hamza, Thomas Moreau, Abderrahim Halimi, and Philippe Ciuciu. "Sparsity-based blind deconvolution of neural activation signal in fMRI." In ICASSP 2019-2019 IEEE International Conference on Acoustics, Speech and Signal Processing (ICASSP), pp. 1323-1327. IEEE, 2019.
21. Cherkaoui, Hamza, Thomas Moreau, Abderrahim Halimi, Claire Leroy, and Philippe Ciuciu. "Multivariate semi-blind deconvolution of fMRI time series." NeuroImage 241 (2021): 118418.
22. Rangaprakash, D., Guo-Rong Wu, Daniele Marinazzo, Xiaoping Hu, and Gopikrishna Deshpande. "Hemodynamic response function (HRF) variability confounds resting-state fMRI functional connectivity." Magnetic resonance in medicine 80, no. 4 (2018): 1697-1713.
23. Caballero Gaudes, César, Natalia Petridou, Susan T. Francis, Ian L. Dryden, and Penny A. Gowland. "Paradigm free mapping with sparse regression automatically detects single-trial functional magnetic resonance imaging blood oxygenation level dependent responses." Human brain mapping 34, no. 3 (2013): 501-518.
24. Karahanoğlu, Fikret Işık, César Caballero-Gaudes, François Lazeyras, and Dimitri Van De Ville. "Total activation: fMRI deconvolution through spatio-temporal regularization." Neuroimage 73 (2013): 121-134.
25. Caballero-Gaudes, César, Stefano Moia, Puja Panwar, Peter A. Bandettini, and Javier Gonzalez-Castillo. "A deconvolution algorithm for multi-echo functional MRI: Multi-echo Sparse Paradigm Free Mapping." Neuroimage 202 (2019): 116081.
26. Gitelman, Darren R., William D. Penny, John Ashburner, and Karl J. Friston. "Modeling regional and psychophysiologic interactions in fMRI: the importance of hemodynamic deconvolution." Neuroimage 19, no. 1 (2003): 200-207.
27. Gaudes, Cesar Caballero, Natalia Petridou, Ian L. Dryden, Li Bai, Susan T. Francis, and Penny A. Gowland. "Detection and characterization of single-trial fMRI bold responses: Paradigm free mapping." Human brain mapping 32, no. 9 (2011): 1400-1418.
28. Uruñuela, Eneko, Thomas AW Bolton, Dimitri Van De Ville, and César Caballero-Gaudes. "Hemodynamic Deconvolution Demystified: Sparsity-Driven Regularization at Work." arXiv preprint arXiv:2107.12026 (2021).
29. Theodoridis, Sergios, and Konstantinos Koutroumbas. Pattern Recognition, 4th Edition. Academic Press, 2009.
30. Mohr, Holger, and Hannes Ruge. "Fast estimation of L1-regularized linear models in the mass-univariate setting." Neuroinformatics 19, no. 3 (2021): 385-392.
31. Auerbach, E. J., Xu, J., Yacoub, E., Moeller, S., & Uğurbil, K. (2013). Multiband accelerated spin-echo echo planar imaging with reduced peak RF power using time-shifted RF pulses. Magnetic resonance in medicine, 69(5), 1261-1267.
32. Ashburner, John, Gareth Barnes, Chun-Chuan Chen, Jean Daunizeau, Guillaume Flandin, Karl Friston, Stefan Kiebel et al. "SPM12 manual." Wellcome Trust Centre for Neuroimaging, London, UK 2464 (2014).
33. Fonov, Vladimir, Alan C. Evans, Kelly Botteron, C. Robert Almli, Robert C. McKinstry, D. Louis Collins, and Brain Development Cooperative Group. "Unbiased average age-appropriate atlases for pediatric studies." Neuroimage 54, no. 1 (2011): 313-327.
34. Parmar, Harshit S., Brian Nutter, Rodney Long, Sameer Antani, and Sunanda Mitra. "Automated signal drift and global fluctuation removal from 4D fMRI data based on principal component analysis as a major preprocessing step for fMRI data analysis." In Medical Imaging 2019: Biomedical Applications in Molecular, Structural, and Functional Imaging, vol. 10953, pp. 300-308. SPIE, 2019.
35. Gonzalez-Castillo, Javier, Ziad S. Saad, Daniel A. Handwerker, Souheil J. Inati, Noah Brenowitz, and Peter A. Bandettini. "Whole-brain, time-locked activation with simple tasks revealed using massive averaging and model-free analysis." Proceedings of the National Academy of Sciences 109, no. 14 (2012): 5487-5492.
36. Mechelli, Andrea, Glyn W. Humphreys, Kate Mayall, Andrew Olson, and Cathy J. Price. "Differential effects of word length and visual contrast in the fusiform and lingual gyri during." Proceedings of the Royal Society of London. Series B: Biological Sciences 267, no. 1455 (2000): 1909-1913.
37. Zahn, Roland, Walter Huber, Eva Drews, Stephan Erberich, Timo Krings, Klaus Willmes, and Michael Schwarz. "Hemispheric lateralization at different levels of human auditory word processing: a functional magnetic resonance imaging study." Neuroscience letters 287, no. 3 (2000): 195-198.
38. Zhu, Linlin, Yang Fan, Qihong Zou, Jue Wang, Jia-Hong Gao, and Zhendong Niu. "Temporal reliability and lateralization of the resting-state language network." PLoS one 9, no. 1 (2014): e85880

39. Tie, Yanmei, Laura Rigolo, Isaiah H. Norton, Raymond Y. Huang, Wentao Wu, Daniel Orringer, Srinivasan Mukundan Jr, and Alexandra J. Golby. "Defining language networks from resting-state fMRI for surgical planning—A feasibility study." Human brain mapping 35, no. 3 (2014): 1018-1030.
40. Pardo, José V., Patricia J. Pardo, Kevin W. Janer, and Marcus E. Raichle. "The anterior cingulate cortex mediates processing selection in the Stroop attentional conflict paradigm." Proceedings of the National Academy of Sciences 87, no. 1 (1990): 256-259.
41. Botvinick, Matthew M. "Conflict monitoring and decision making: reconciling two perspectives on anterior cingulate function." Cognitive, Affective, & Behavioral Neuroscience 7, no. 4 (2007): 356-366.
42. Walton, Mark E., Paula L. Croxson, Timothy EJ Behrens, Steven W. Kennerley, and Matthew FS Rushworth. "Adaptive decision making and value in the anterior cingulate cortex." Neuroimage 36 (2007): T142-T154.
43. Rombouts, Serge ARB, Frederik Barkhof, Rutger Goekoop, Cornelis J. Stam, and Philip Scheltens. "Altered resting state networks in mild cognitive impairment and mild Alzheimer's disease: an fMRI study." Human brain mapping 26, no. 4 (2005): 231-239.
44. Cole, Michael W., Jeremy R. Reynolds, Jonathan D. Power, Grega Repovs, Alan Anticevic, and Todd S. Braver. "Multi-task connectivity reveals flexible hubs for adaptive task control." Nature neuroscience 16, no. 9 (2013): 1348-1355.
45. Dove, Anja, Stefan Pollmann, Torsten Schubert, Christopher J. Wiggins, and D. Yves Von Cramon. "Prefrontal cortex activation in task switching: an event-related fMRI study." Cognitive brain research 9, no. 1 (2000): 103-109.
46. Arulpragasam, Amanda R., Jessica A. Cooper, Makiah R. Nuutinen, and Michael T. Treadway. "Corticoinsular circuits encode subjective value expectation and violation for effortful goal-directed behavior." Proceedings of the National Academy of Sciences 115, no. 22 (2018): E5233-E5242.
47. Pezzulo, Giovanni, Francesco Rigoli, and Karl J. Friston. "Hierarchical active inference: a theory of motivated control." Trends in cognitive sciences 22, no. 4 (2018): 294-306.